Available online at www.sciencedirect.com
ScienceDirect
Journal of Catalysis 247 (2007) 245–255
JOURNAL OF CATALYSIS
www.elsevier.com/locate/jcat

SBA-15-supported molybdenum oxides as efficient catalysts for selective oxidation of ethane to formaldehyde and acetaldehyde by oxygen

Yinchuan Lou, Huichun Wang, Qinghong Zhang, Ye Wang *

State Key Laboratory of Physical Chemistry of Solid Surfaces, College of Chemistry and Chemical Engineering, Xiamen University, Xiamen 361005, China

Received 7 December 2006; revised 5 February 2007; accepted 12 February 2007

Available online 23 March 2007

Abstract

The selective oxidation of ethane was investigated over SBA-15-supported molybdenum oxide catalysts. Our characterizations suggest that the MoO_x species were dispersed mostly in mesoporous channels of SBA-15 at Mo content <9.5 wt%. At higher Mo content (15.4 and 20.1 wt%), MoO_x nanoparticles together with small amount of MoO_3 crystallites were found. The growth of MoO_x species in mesoporous channels to MoO_x nanoparticles causes the collapse of the silica wall of SBA-15. The rate of ethane conversion per Mo atom over the catalyst with Mo content of 9.5–20.1 wt% was significantly higher than that over the catalyst with lower Mo content, suggesting that polymeric MoO_x clusters and MoO_x nanoparticles are more active toward ethane activation. The catalysts with highly dispersed MoO_x species favor the selectivity of acetaldehyde, whereas those containing polymeric MoO_x clusters or MoO_x nanoparticles show higher formaldehyde formation rates. Formaldehyde is likely produced through the consecutive oxidation of ethylene.

Keywords: Molybdenum oxide; SBA-15; Selective oxidation; Ethane; Formaldehyde; Acetaldehyde

1. Introduction

The selective oxidation of lower alkanes (particularly CH_4 and C_2H_6, which are major components of natural gas) into valuable oxygenates is one of the most challenging research areas in catalysis. A number of studies have shown that silica-supported molybdenum oxide can catalyze the selective oxidation of CH_4 to HCHO by O_2 with a relatively high efficiency among various heterogeneous catalysts [1–8]. However, whether the supported MoO_x catalysts are effective in the selective oxidation of C_2H_6 by O_2 to oxygenates such as CH_3CHO is ambiguous [9,10]. Mendelovici and Lunsford [11] reported a relatively high selectivity to CH_3CHO (∼37% at a C_2H_6 conversion of ∼4%) during the oxidation of C_2H_6 by N_2O in the presence of steam at 825 K over a 2 wt% MoO_x/SiO_2 catalyst prereduced by CO. Solymosi and co-workers [12] studied the selective oxidation of C_2H_6 by N_2O over silica-supported alkali metal molybdate catalysts and found that the K_2MoO_4/SiO_2 showed the highest activity for CH_3CHO formation (27% selectivity at 7.3% conversion at 823 K). Research reports on the selective oxidation of C_2H_6 by O_2 over the supported MoO_x catalysts are unexpectedly scarce, although there are some papers on catalytic properties of supported VO_x catalysts for the conversion of C_2H_6 to oxygenates by O_2 [13–16]. Otsuka et al. [17] reported that the activity of MoO_x/SiO_2 for the oxidation of C_2H_6 by O_2 was almost the same as that of pure silica. Although the reactivity of the supported MoO_x catalysts in the oxidative dehydrogenation of C_2H_6 has been mentioned in a few studies [18], their performance in the selective oxidation of C_2H_6 to organic oxygenates by O_2 is not very clear.

Many studies have investigated the structure of active species for the selective oxidation of CH_4 to HCHO by O_2 over the MoO_x/SiO_2 catalysts. Most of these studies suggested that the highly dispersed MoO_x species such as the monomeric MoO_x (or mono-molybdate) species or the silicomolybdates account for the activation of CH_4 by O_2 and the formation of HCHO [19–25]. For the selective oxidation of C_2H_6 by N_2O over the MoO_x/SiO_2 catalyst, the isolated Mo^V sites generated after prereduction with CO have been proposed as the active sites [11]. However, few papers have addressed the structure

* Corresponding author. Fax: +86 592 2183047.
E-mail address: wangye@xmu.edu.cn (Y. Wang).

0021-9517/$ – see front matter
doi:10.1016/j.jcat.2007.02.011

of active MoO_x species for the selective oxidation of C_2H_6 by O_2 [10]. On the other hand, the structure–reactivity relationships for the oxidative dehydrogenation of C_3H_8 by O_2 have been studied in detail over some supported MoO_x catalysts [26,27]. It has been reported that within a Mo surface density range of 0.4–4.5 Mo nm^{-2}, the C_3H_8 conversion rate per Mo atom increases with a decrease in the UV absorption edge energy, and thus increases with a rise in the domain size of the MoO_x species supported on Al_2O_3 [26,27]. These studies imply that different structure of MoO_x species may be required for the conversion of different alkanes and the formation of different products.

The main purposes of the present work are to investigate the catalytic properties of the supported MoO_x catalyst in the selective oxidation of C_2H_6 by O_2 and to gain insight into the structural requirements for the conversion of C_2H_6 and the formation of selective oxidation products, especially the organic oxygenates. We have chosen SBA-15 (a typical mesoporous silica) as the support of MoO_x species in our work because SBA-15 has large surface areas and ordered nanosize spaces (mesoporous channels) to allow high dispersion and tailoring of the active species. Moreover, the relatively thicker walls and the higher thermal stability of SBA-15 make it a promising catalyst support for reactions at high temperatures [28]. Some recent studies have shown that SBA-15 has advantages over other silica-based supports for the selective oxidation of lower alkanes, possibly because of its larger pore diameter ($\geqslant$5 nm) and more inert property (without any acidic sites), which allow the rapid desorption of the partial oxidation products [29–32]. In a previous paper [33], we reported that the SBA-15-supported MoO_x catalyst is more efficient than the Cab-O-Sil- and MCM-41-supported MoO_x catalysts for the selective oxidation of CH_4 to HCHO by O_2.

2. Experimental

2.1. Catalyst preparation

SBA-15 was synthesized by a procedure similar to that described previously [28]. In brief, Pluronic P123 triblock copolymer ($EO_{20}PO_{70}EO_{20}$, Aldrich) and tetraethyl orthosilicate (TEOS) were used as the template and silicon source, respectively. A homogeneous mixture containing $EO_{20}PO_{70}EO_{20}$ and TEOS in hydrochloric acid solution with an $EO_{20}PO_{70}EO_{20}$:TEOS:HCl (2 mol dm^{-3}) weight ratio of 9.6:20.4:227 was first stirred in a round flask at 313 K for 20 h. Then the resultant gel was transferred to a Teflon bottle, which was placed in a stainless steel autoclave. After hydrothermal treatment at 373 K for 24 h, the solid product was recovered by filtration, followed by washing with deionized water and drying at 323 K in vacuum. Powdery SBA-15 was obtained by calcination at 823 K for 6 h in air to remove the organic template.

Molybdenum species were introduced into SBA-15 by an impregnation method [33]. The powdery SBA-15 was immersed into an aqueous solution of ammonium heptamolybdate (i.e., $(NH_4)_6Mo_7O_{24}$), followed by stirring for 8 h. Then water was evaporated with continuous stirring at 323 K. After further drying in vacuum at 323 K for 10 h, the powdery product was subjected to calcination at 873 K for 6 h in air.

2.2. Catalyst characterization

The Mo content (calculated using the wt% of MoO_3) in each sample was determined by inductively coupled plasma (ICP) optical emission spectrometry using an Agilent ICP-MS 4500–300 after the sample was completely dissolved in an alkaline medium. N_2 sorption at 77 K was carried out with a Micromeritics TriStar 3000 surface area and porosimetry analyzer to evaluate the porous properties and the surface areas of each sample. The sample was pretreated at 573 K in vacuum for 3 h before N_2 adsorption. The surface area was calculated by the BET method, and the pore diameter distribution was evaluated by the BJH method.

Powder X-ray diffraction (XRD) patterns were measured with a Panalytical X'Pert Pro Super X-ray diffractometer equipped with X'Celerator and Xe detection systems. CuK_α radiation (40 kV and 30 mA) was used as the X-ray source.

Diffuse reflectance UV–visible (UV–vis) spectra were recorded on a Varian-Cary 5000 spectrometer equipped with a diffuse reflectance accessory. The spectra were collected at 200–800 nm with $BaSO_4$ as a reference.

Laser Raman spectroscopic measurements were carried out with a Renishaw 1000R Raman system. A laser at 514.5 nm was used as the excitation source. The laser output was 30 mW, and the maximum incident power at the sample was approximately 6 mW in each measurement.

Transmission electron microscopy (TEM) was done using a FEI Tecnai 30 electron microscope (Phillips Analytical) operated at an acceleration voltage of 300 kV. Samples for TEM measurements were suspended in ethanol and dispersed ultrasonically. Drops of the suspensions were applied on a copper grid coated with carbon. Scanning electron microscopy (SEM) was done using a LEO1530 scanning electron microscope with 20-kV accelerating voltage.

H_2 temperature-programmed reduction (H_2-TPR) was performed using an Micromeritics AutoChem 2920 II instrument. Typically, the sample loaded in a quartz reactor was first pretreated with a gas flow containing O_2 and He at 823 K for 1 h, followed by purging with pure He at the same temperature for 1 h. After cooling to 303 K, a H_2–Ar gas mixture (5% H_2) was introduced into the reactor, and the temperature was raised to 1200 K at a rate of 10 K min^{-1}. H_2 consumption was monitored by a thermal conductivity detector. The detector response was calibrated using the reduction of CuO powder.

2.3. Catalytic reaction

The catalytic reactions were carried out in a fixed-bed flow reactor operated at atmospheric pressure. The catalyst was pretreated in the quartz reactor (8 mm i.d.) with a gas flow containing high-purity N_2 and O_2 at 873 K for 0.5 h, followed by purging with the high-purity N_2 at the same temperature as before the reaction. The reaction was started by introducing a reactant gas flow containing C_2H_6, O_2, and N_2 (for dilution)

to the reactor at a fixed reaction temperature. The products were analyzed by online gas chromatography. All of the lines and valves between the exit of the reactor and the gas chromatographs were heated to 393 K, to prevent condensation of the products. Organic oxygenates in the products, including HCHO and CH_3CHO, were separated with a Porapak T column and detected using a thermal conductivity detector. The separation of other components, such as O_2, C_2H_6, C_2H_4, CO, and CO_2, were carried out by Porapak Q and Molecular Sieve 5 A columns.

3. Results

3.1. Structural characteristics of MoO_x/SBA-15 catalysts

The Mo contents of the catalysts (wt% of MoO_3) as determined by ICP are given in Table 1. The final Mo content in each catalyst was almost the same as that used in synthesis, indicating that the loss of Mo was negligible during high-temperature calcination (at 873 K). Table 1 also summarizes surface areas, pore volumes, and pore diameters of the MoO_x/SBA-15 catalysts obtained from N_2-sorption at 77 K. Mo surface density (i.e., number of Mo atoms per square nanometer BET surface area) was evaluated from the Mo content and surface area. Surface areas decreased gradually with increasing Mo content from 2.8 to 9.5 wt%, but a significant drop occurred as Mo content rose from 9.5 to 15.4 wt%. Accompanying this drop, the pore diameter underwent a sudden increase from ∼6.5 to ∼20 nm. Further increases in Mo content had only a slight affect on the surface area and the pore diameter.

Fig. 1 shows the adsorption–desorption isotherms for SBA-15 and 9.5 and 15.4 wt% MoO_x/SBA-15 samples. SBA-15 and 9.5 wt% MoO_x/SBA-15 samples exhibited the type-IV isotherms and the type-H1 hysteresis loops typical for mesoporous materials with cylindrical porous channels [28]. For these two samples, the capillary condensation occurred at a relative pressure (p/p^0) of ∼0.7, and the pore diameters estimated using the BJH analysis were 6.3 and 6.7 nm, respectively. These features are consistent with those reported by Zhao et al. [28] for SBA-15 alone. On the other hand, for the 15.4 wt% MoO_x/SBA-15 sample, the isotherms changed significantly; the step for capillary condensation shifted to a significantly higher p/p^0, and the amount of adsorbed N_2 decreased. These observations suggest the collapse of the mesoporous structure in this sample. We speculate that the significantly larger pore diameters (∼20 nm) of the MoO_x/SBA-15 samples with Mo content >15.4 wt% probably arose from stacking of the pores by nanoparticles.

Table 1
Physical properties of the MoO_x/SBA-15 catalysts with different Mo content

Mo content[a] (in synthesis) (wt%)	Mo content[a] (by ICP) (wt%)	Surface area ($m^2\ g^{-1}$)	Mo surface density[b] (Mo nm^{-2})	Pore volume ($cm^3\ g^{-1}$)	Pore diameter (nm)
0	0	627	0	0.82	6.3
3.0	2.8	460	0.25	0.74	6.3
5.0	4.9	463	0.45	0.75	6.3
7.0	6.6	447	0.61	0.72	6.4
10	9.5	369	1.08	0.67	6.7
15	15.4	119	5.41	0.61	19.2
20	20.1	111	7.56	0.60	20.5
25	23.5	96	10.24	0.55	20.9

[a] Mo content is calculated by the weight percentage of MoO_3 in the sample.
[b] Mo surface density is calculated from the Mo content and the surface area.

The change in mesoporous structure with Mo content was also demonstrated by XRD patterns at low diffraction angles. SBA-15 exhibited three distinct diffraction peaks at 0.97°, 1.63°, and 1.88° that can be assigned to (100), (110), and (200) reflections associated with p6mm hexagonal symmetry [28]. The increase in Mo content up to 9.5 wt% did not affect these peaks significantly, but a further increase in Mo content to 15.4 wt% caused the disappearance of all three diffraction peaks.

Fig. 2 shows that no XRD peaks corresponding to Mo compounds can be detected in the catalysts with Mo content <9.5 wt%, suggesting that the MoO_x species probably were

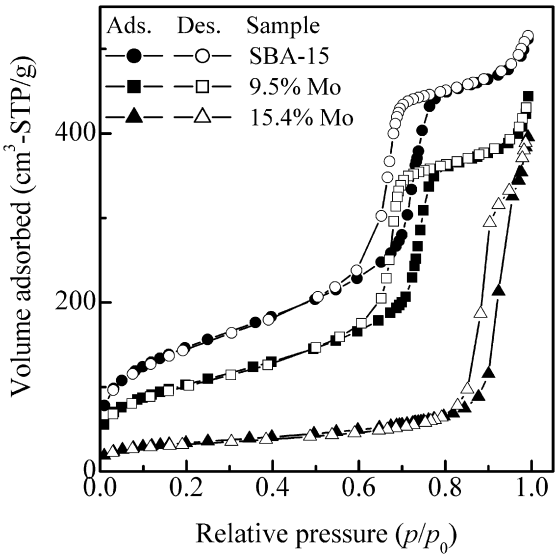

Fig. 1. N_2-sorption isotherms of SBA-15, 9.5 wt% MoO_x/SBA-15, and 15.4 wt% MoO_x/SBA-15.

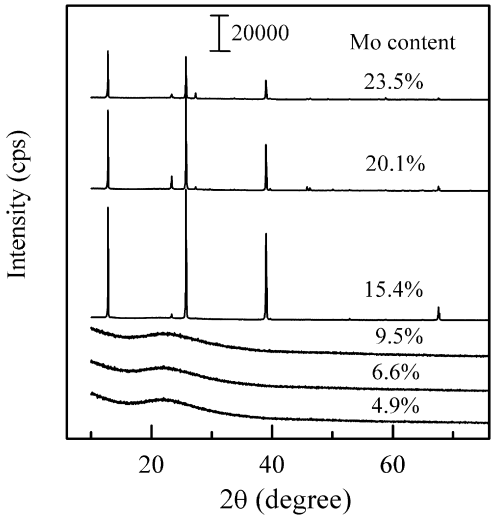

Fig. 2. XRD patterns of MoO_x/SBA-15 catalysts with different Mo content.

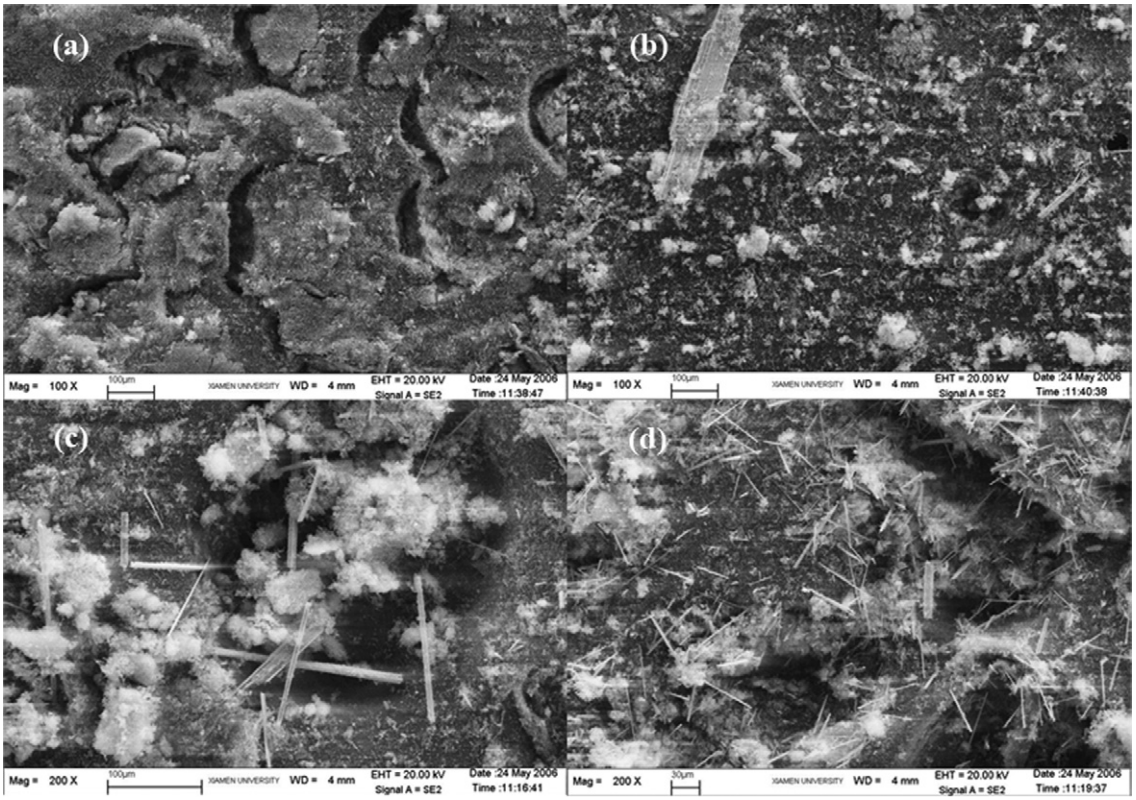

Fig. 3. SEM images of MoO_x/SBA-15 catalysts with different Mo content: (a) 9.5, (b) 15.4, (c) 20.1, and (d) 23.5 wt%. The scale bar is 100 μm in (a), (b), and (c) and 30 μm in (d).

highly dispersed in the mesoporous channels of SBA-15. Strong diffraction peaks of crystalline MoO_3 were observed as Mo content rose to 15.4 wt%, demonstrating the appearance of MoO_3 crystallites. The intensity of the diffraction lines ascribed to MoO_3 did not increase, but rather decreased with further increases in Mo content. To gain further information about the MoO_3 crystallites in the catalysts, we investigated the morphological change with Mo content by SEM. The results, shown in Fig. 3, indicate that large MoO_3 crystallites did not exist in the catalyst with a Mo content of 9.5 wt%, consistent with the XRD pattern. Plate-like and belt-like MoO_3 crystallites appeared in the 15.4 wt% MoO_x/SBA-15, but the number of such crystallites was very limited in this sample. Belt-like crystallites were observed mainly in the sample with a Mo content of 20.1 wt%, and a number of thin, needle-like MoO_3 crystallites were formed in the 23.5 wt% MoO_x/SBA-15. Thus, the morphology of MoO_3 crystallites changed with Mo content from 15.4 to 23.5 wt%. It is speculated that the higher intensity of the XRD peaks for the 15.4 wt% MoO_x/SBA-15 sample may stem from the small amount of the larger plate-like or belt-like MoO_3 crystallites in this sample.

Raman spectra for the MoO_x/SBA-15 samples after dehydration at 873 K in O_2 flow are shown in Fig. 4. SBA-15 exhibited broad and weak bands at 607, 810, and 1020 cm^{-1}, which can be assigned to the surface hydroxyl groups, the siloxane linkage, and the siloxane rings, respectively [34]. For the sample with a very low Mo content (0.9 wt%), a broad band at 970 cm^{-1} was detected in addition to those for SBA-15 alone.

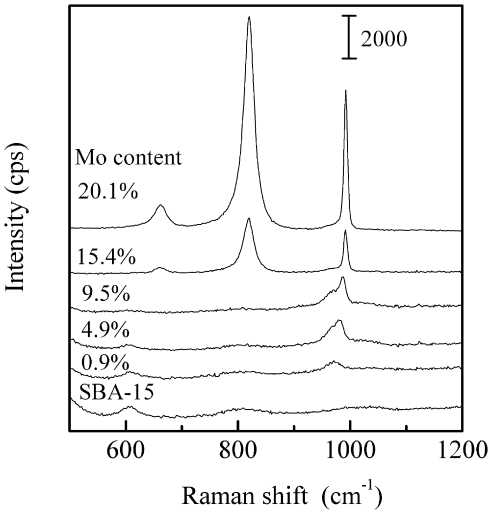

Fig. 4. Raman spectra of MoO_x/SBA-15 catalysts with different Mo content after treatment in O_2 at 873 K for 1 h.

With increasing Mo content to 4.9 and 9.5 wt%, along with the band at 970 cm^{-1}, a band at 980–985 cm^{-1} also could be discerned, although the two bands were overlapped. The same phenomenon has been reported for the MoO_x/SiO_2 catalysts under dehydration conditions [34]. The band at around 980 cm^{-1} could be assigned to the stretching vibration of terminal Mo=O of highly dispersed MoO_x species, such as monomeric MoO_x moieties and small MoO_x oligomers or clusters [26,34], whereas that at 970 cm^{-1} might be ascribed to

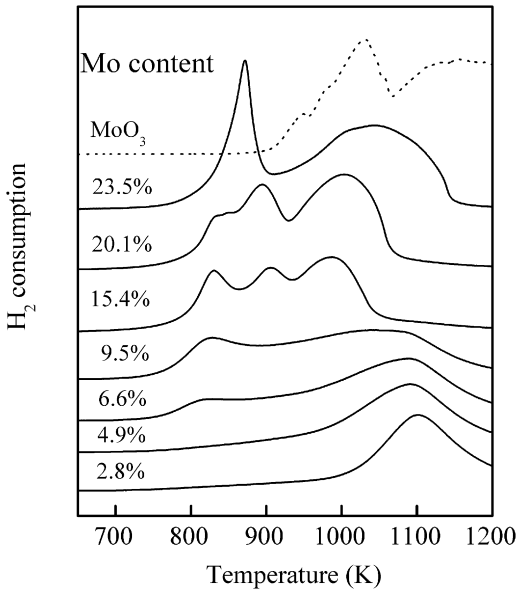

Fig. 5. H_2-TPR profiles of MoO_x/SBA-15 catalysts with different Mo content.

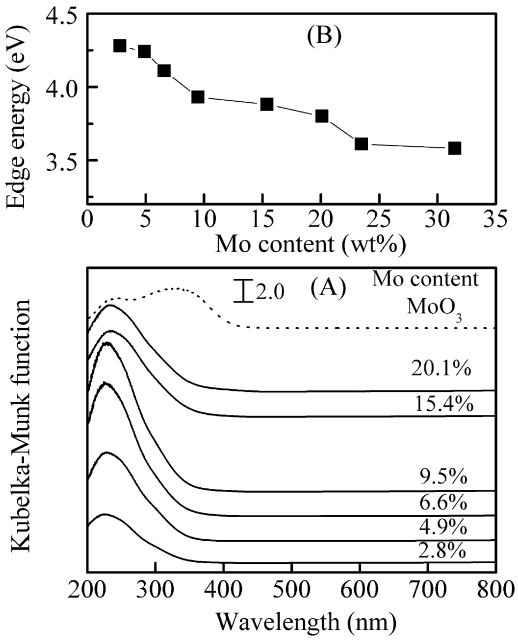

Fig. 6. Diffuse reflectance UV–vis spectra (A) and edge energy values (B) for MoO_x/SBA-15 catalysts with different Mo content.

a highly dispersed surface molybdenum species with interaction with SiO_2. The absence of Mo–O–Mo stretching in these samples is consistent with the absence of crystalline molybdenum oxide in their XRD patterns and SEM images. This further suggests that the samples with Mo content of <9.5 wt% contain mainly highly dispersed MoO_x species. With increasing Mo content to 15.4 wt% and above, Raman bands of crystalline MoO_3 at 992, 820, and 660 cm^{-1} were clearly observed.

Fig. 5 shows H_2-TPR profiles of the MoO_x/SBA-15 catalysts with various Mo contents. To make a better comparison, the amount of Mo in each sample was maintained in all experiments by varying the amount of each catalyst. For the sample with a lower Mo content (2.8 or 4.9 wt%), only a reduction peak at a higher temperature (1080–1110 K) was observed. The increase in Mo content to 6.6 and 9.5 wt% led to the appearance of another reduction peak at ~830 K. It is reasonable to speculate that the high-temperature peak at 1080–1110 K corresponds to the reduction of the monomeric MoO_x species, which may have interactions with SBA-15, whereas the reduction peak at ~830 K probably arises from the oligomeric MoO_x species or small MoO_x clusters. Further increases in Mo content changed the reduction profile significantly. The peak at 1080–1110 K disappeared, but two other peaks at 905 and 985 K were observed for the 15.4 wt% MoO_x/SBA-15 sample. As the Mo content increased from 15.4 to 20.1 wt%, these two peaks shifted slightly to lower and higher temperatures, respectively. We speculate that these reduction peaks might be ascribed to MoO_x nanoparticles and MoO_3 crystallites, respectively. A further increase in Mo content to 23.5 wt% further changed the TPR profile; a sharp peak at 872 K was observed, along with a very broad peak beginning at ~910 K. These two peaks may also be assigned to the reduction of MoO_x nanoparticles and MoO_3 crystallites.

For supported MoO_x samples, the position of the UV–vis absorption edge for charge-transfer transitions is known to reflect the average size of MoO_x domains [26,35]. Fig. 6A shows the diffuse reflectance UV–vis spectra of MoO_x/SBA-15 samples with different Mo contents. MoO_3 exhibited two overlapped absorption bands, at 242 and 330 nm. The MoO_x/SBA-15 samples with Mo content lower than 9.5 wt% showed an absorption band in the UV region with peak position at ~227 nm. With increasing Mo content to 15.4 wt% and above, the peak position of the band shifted to ~235 nm and the absorption edge also shifted to a longer-wavelength position. We calculated the edge energy from the UV–vis spectra using the method proposed by Weber [35], by finding the energy intercept of the straight line in the plot of $[F(R_\infty) \times h\upsilon]^2$ against $h\upsilon$, where $F(R_\infty)$ is the Kubelka–Munk function and $h\upsilon$ is the incident photon energy. As shown in Fig. 6B, the calculated values for the MoO_x/SBA-15 samples with Mo contents of 2.8 and 4.9 wt% (4.2–4.3 eV) were close to those for the isolated mononuclear molybdate moieties [35], indicating that these two samples are dominated by monomeric MoO_x species. The edge energy decreased significantly with increasing Mo content from 4.9 to 9.5 wt%, corresponding to the simultaneous increase in the average domain size of MoO_x species. Thus, the monomeric MoO_x species likely aggregated to MoO_x oligomers or polymeric MoO_x clusters as Mo content increased from 4.9 to 9.5 wt%. This finding is consistent with the analysis of H_2-TPR results described above. With further increases in Mo content from 9.5 to 20.1 wt%, the edge energy decreased only slightly. In these samples, the dominant Mo species likely were the polymeric MoO_x clusters or MoO_3 nanoparticles. A drop in edge energy was observed as Mo content was raised further from 20.1 to 23.5 wt%, consistent with the presence of a larger number of needle-like MoO_3 crystallites.

As observed from N_2-sorption and XRD measurements, the mesoporous structure of SBA-15 was destroyed as Mo content rose to 15.4 wt%. We could see large plate-like or belt-like

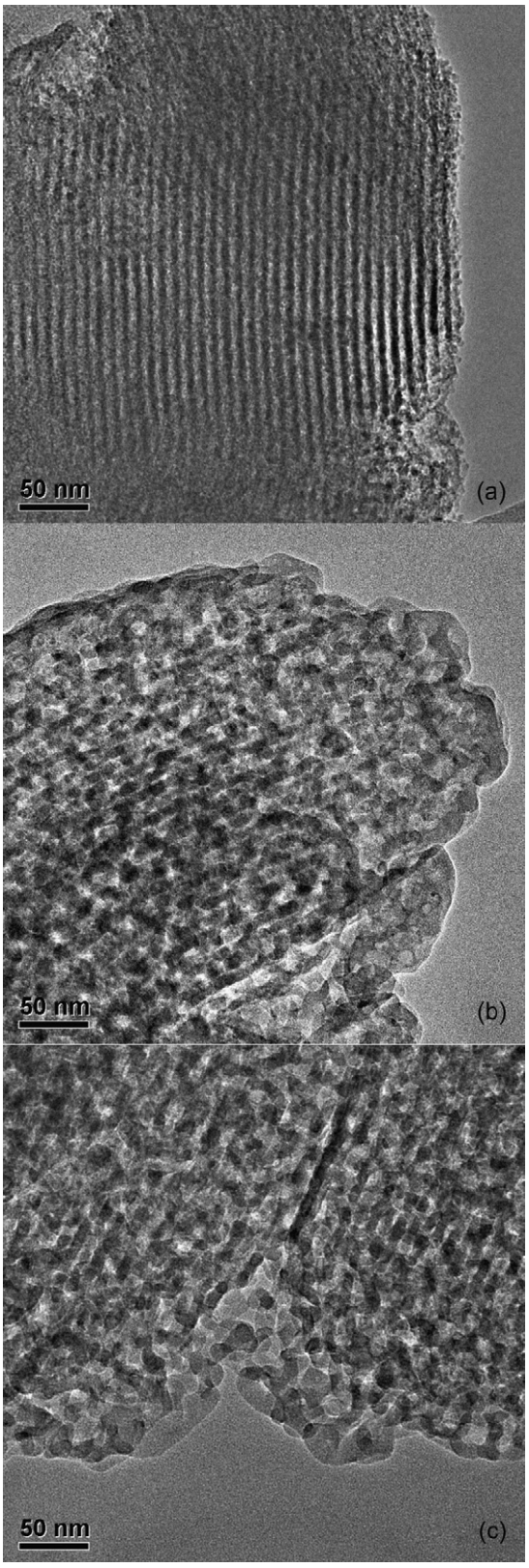

Fig. 7. TEM images of MoO_x/SBA-15 catalysts with different Mo content: (a) 9.5, (b) 15.4, and (c) 20.1 wt%.

MoO_3 crystallites in the SEM image of this sample, but these crystallites were not numerous. Moreover, the average size of MoO_x domains estimated from UV–vis spectra increased

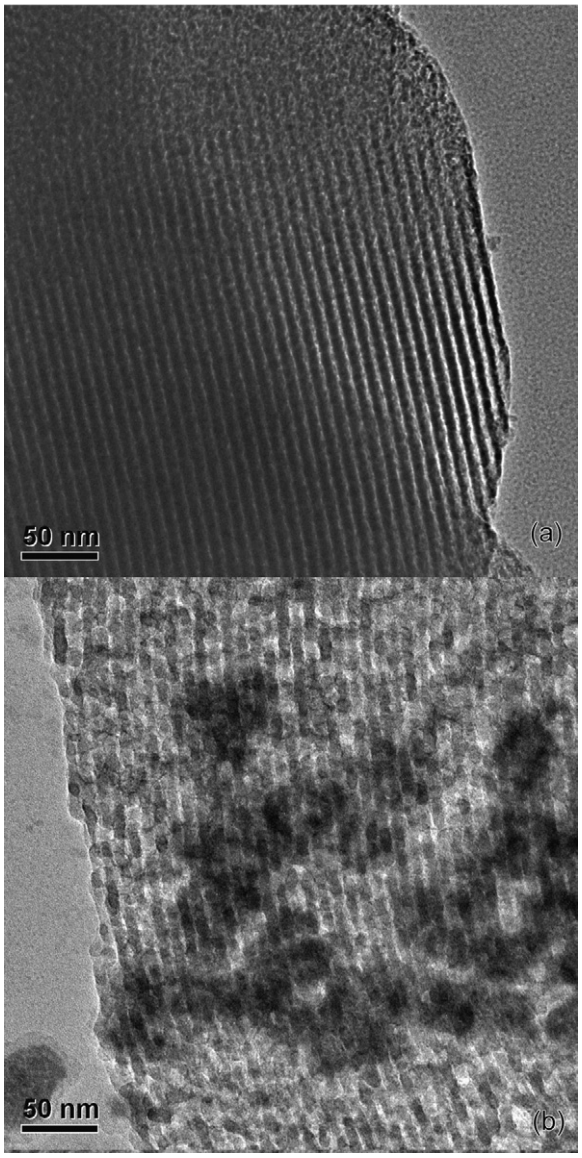

Fig. 8. TEM images of the 20.1 wt% MoO_x/SBA-15 samples calcined at different temperatures: (a) 823 and (b) 848 K.

only slightly as Mo content rose from 9.5 to 15.4 and then to 20.1 wt%. We performed TEM experiments to obtain further information about the changes in mesoporous structure and MoO_x species. As shown in Fig. 7, the ordered mesoporous structure was sustained for the 9.5 wt% MoO_x/SBA-15 sample, coinciding with the N_2-sorption and XRD results. As Mo content increased to 15.4 and 20.1 wt%, collapse of the silica wall of SBA-15 occurred. MoO_x nanoparticles of ∼10–20 nm can be observed in the TEM images of these two samples. This implies that the growth of MoO_x species inside the mesoporous channels into MoO_x nanoparticles probably destroyed the silica wall of SBA-15.

To confirm this speculation, we studied the 20.1 wt% MoO_x/SBA-15 samples calcined at different temperatures with TEM; the images are shown in Fig. 8. The sample calcined at 823 K exhibited well-ordered mesoporous channels and showed few MoO_x nanoparticles. The growth of MoO_x species to nanoparticles along the porous direction and the unlinking of

the silica wall in some places were seen in the sample calcined at 848 K, although the long-range order of mesoporous channels was maintained. The silica wall was completely destroyed due to the further growth of MoO_x nanoparticles after calcination at 873 K (Fig. 7c). Therefore, although large plate-like or belt-like MoO_3 crystallites also were observed in the 15.4 and 20.1 wt% MoO_3/SBA-15 samples by SEM, UV–vis and TEM suggest that the polymeric MoO_x clusters and MoO_x nanoparticles were dominant in these samples.

3.2. Catalytic behavior of MoO_x /SBA-15 catalysts

Fig. 9 shows the dependence of the catalytic behavior of the MoO_x/SBA-15 catalysts on Mo content at 873 K for the selective oxidation of C_2H_6 by O_2. Under our reaction conditions, the blank test showed that the conversion of C_2H_6 was < 1%. SBA-15 gave a very low C_2H_6 conversion (1.6%) at 873 K, and C_2H_4 was the main product (selectivity, 86%). With increasing Mo content up to 6.6 wt%, C_2H_6 conversion increased gradually. The selectivity of CH_3CHO increased significantly from ∼3 to ∼20% with the presence of even a small amount of molybdenum species on SBA-15 (2.8 wt%). The increase in Mo content from 2.8 to 6.6 wt% increased the CH_3CHO selectivity slightly.

Further increases in Mo content exceeding 6.6 wt% caused a steep rise in C_2H_6 conversion. C_2H_6 conversion reached a maximum at a Mo content of 20.1 wt% and then decreased with a further increase in Mo content to 23.5 wt%. The selectivity of CH_3CHO decreased significantly as the Mo content exceeded 6.6 wt%. However, it is of interest to note that the selectivity of HCHO increased significantly from ∼10 to ∼30% with an increase in Mo content from 6.6 to 15.4 wt%. Further increases in Mo content did not alter the HCHO selectivity. The highest yield of HCHO (4.2%) was achieved over the 20.1 wt% MoO_x/SBA-15 catalyst; on the other hand, the highest yield of CH_3CHO (0.94%) was obtained over the catalyst with a Mo content of 9.5 wt%. Considering the yield to both oxygenates (i.e., the sum of HCHO and CH_3CHO), the 20.1 wt% MoO_x/SBA-15 was the best catalyst, providing a yield of 4.7% at 873 K.

The calculated rates per Mo atom for the conversion of C_2H_6 and the formation of CH_3CHO and HCHO at 873 K are shown in Fig. 10. The rate of C_2H_6 conversion decreased slightly as Mo content rose from 2.8 to 6.6 wt% but underwent a steep increase with a rise in Mo content from 6.6 to 9.5 wt%. Further increases in Mo content from 9.5 to 20.1 wt% decreased the rate of C_2H_6 conversion only slightly. With increasing Mo content, the rate of CH_3CHO formation remained almost unchanged at a Mo content of 2.8–9.5 wt%, but then decreased significantly. In contrast, the rate of HCHO formation increased sharply as Mo content rose from 6.6 to 15.4 wt% and reached a maximum at a Mo content of 15.4 wt%. The 20.1 wt% MoO_x/SBA-15 catalyst exhibited a comparable rate of HCHO formation as the 15.4 wt% MoO_x/SBA-15 catalyst, but the 23.5 wt% MoO_x/SBA-15 catalyst showed a significantly lower rate of HCHO formation.

Although the formation of HCHO has been reported in the oxidation of C_2H_6 over a few catalysts, such as Cs-modified VO_x/SiO_2, $FePO_4$, and SBA-15-supported potassium [14,36–38], the selectivity and yield to HCHO in these studies are <15 and 1.5%, respectively. Over our 20.1 wt% MoO_x/SBA-15 catalyst, HCHO selectivity of ∼30% and yield of ∼4% can be obtained. We have studied the stability of this catalyst. As shown

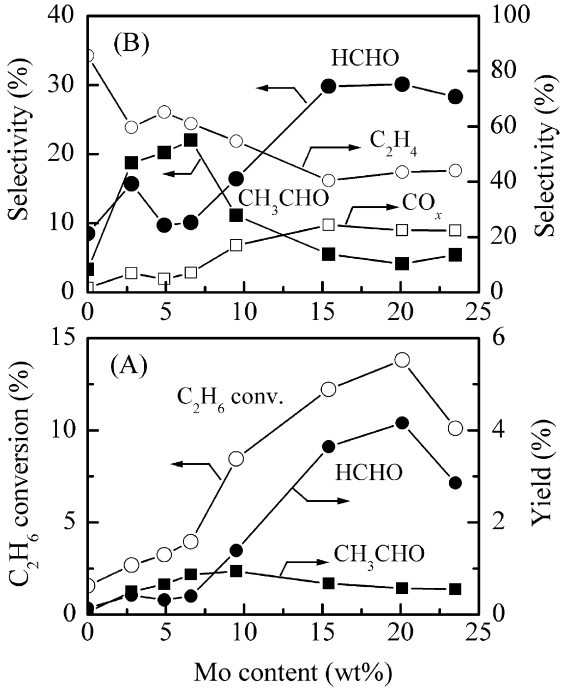

Fig. 9. Dependence of catalytic behaviors of MoO_x/SBA-15 catalysts on Mo content for selective oxidation of ethane by O_2. Reaction conditions: catalyst, 0.2 g; temperature, 873 K; total flow rate, 150 $cm^3\ min^{-1}$; partial pressures of C_2H_6 and O_2, 10.1 kPa.

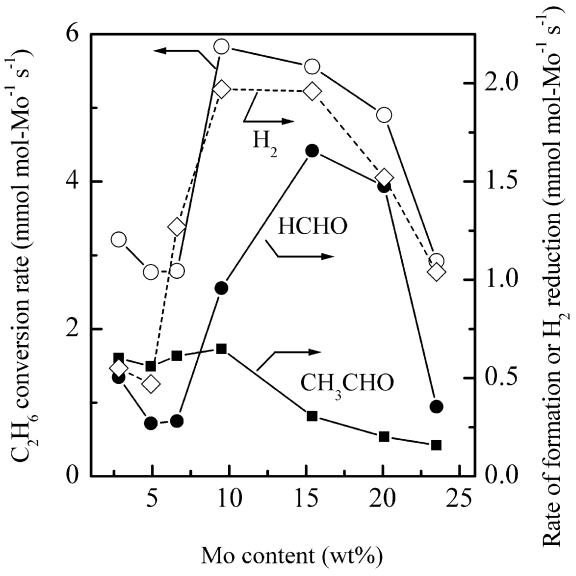

Fig. 10. Dependence of rates per Mo atom for C_2H_6 conversion, product formation, and H_2 reduction over MoO_x/SBA-15 catalysts on Mo content. Reaction conditions: catalyst, 0.2 g; temperature, 873 K; total flow rate, 150 $cm^3\ min^{-1}$; partial pressures of C_2H_6 and O_2, 10.1 kPa. H_2 reduction rates were calculated from Fig. 5.

Table 2
Catalytic performances of the 20.1 wt% MoO_x/SBA-15 for the selective oxidation of ethane by O_2 under different temperatures[a]

T (K)	Conversion (%)	Selectivity (%)					Yield (%)	
		CH_3CHO	HCHO	C_2H_4	CO	CO_2	CH_3CHO	HCHO
823	0.90	22	20	48	8.4	2.2	0.20	0.18
848	4.9	12	28	41	15	3.5	0.61	1.4
863	11	7.0	28	39	21	4.8	0.75	3.0
873	14	4.1	30	44	17	5.0	0.57	4.2

[a] Reaction conditions: catalyst, 0.2 g; total flow rate, 150 $cm^3\ min^{-1}$; partial pressures of C_2H_6 and O_2, 10.1 kPa.

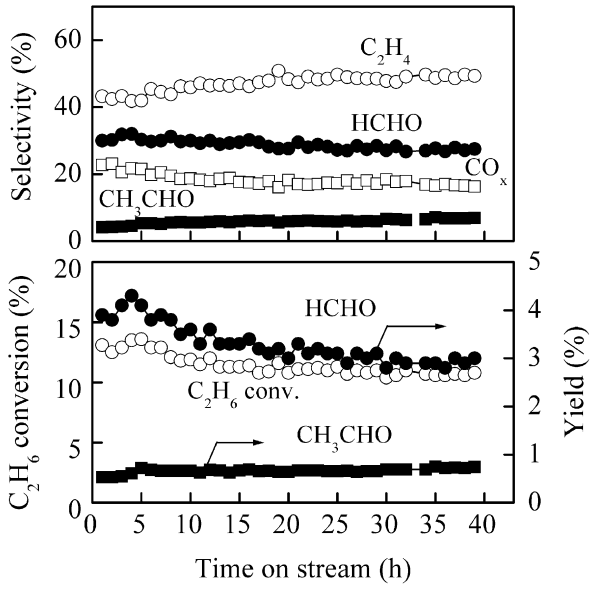

Fig. 11. Changes of catalytic performances with time on stream for the oxidation of C_2H_6 over the 20.1 wt% MoO_x/SBA-15 catalyst. Reaction conditions: catalyst, 0.2 g; temperature, 873 K; total flow rate, 150 $cm^3\ min^{-1}$; partial pressures of C_2H_6 and O_2, 10.1 kPa.

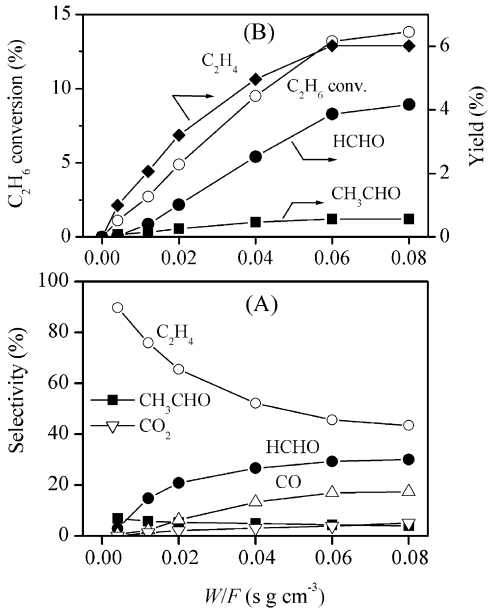

Fig. 12. Effect of contact time on catalytic performances of the 20.1 wt% MoO_x/SBA-15 catalyst in selective oxidation of ethane by O_2. Reaction conditions: temperature, 873 K; partial pressures of C_2H_6 and O_2, 10.1 kPa.

in Fig. 11, in the initial 5 h, HCHO yield can be maintained at ∼4%. With increased time on stream to ∼40 h, C_2H_6 conversion and HCHO selectivity decreased only slightly, from 14 and 30% to 11 and 28%, respectively. Thus, an HCHO yield of 3.0% can still be obtained after ∼40 h of reaction. At the same time, we can obtain a CH_3CHO yield of 0.75%. Therefore, the 20.1 wt% MoO_x/SBA-15 is an attractive catalyst for the selective oxidation of C_2H_6 by O_2 to yield HCHO. To gain information about the reaction paths for the formation of HCHO as well as CH_3CHO, we have investigated in detail the selective oxidation of C_2H_6 over the 20.1 wt% MoO_x/SBA-15 catalyst.

The effect of reaction temperature on C_2H_6 conversion and product selectivities over the 20.1 wt% MoO_x/SBA-15 catalyst is shown in Table 2. C_2H_6 conversion increased exponentially with temperature, and the calculation based on Arrhenius plot gave an apparent activation energy of 350 kJ mol^{-1}. CH_3CHO could be formed with a higher selectivity at a lower temperature, and selectivity decreased with increasing temperature. The selectivity to C_2H_4 also showed a trend to decrease with increasing temperature (except for 873 K), whereas selectivity to HCHO, CO, and CO_2 increased. These observations may suggest that HCHO is produced as a secondary product from C_2H_4 or CH_3CHO.

To further clarify this point, we investigated the effect of pseudo-contact time, W/F, on catalytic performance at 873 K, where W is the catalyst weight and F is the total flow rate. Our result (Fig. 12) shows that the shorter contact time favors the selectivity of C_2H_4 and CH_3CHO, whereas those to HCHO and CO increase with increasing contact time. This observation suggests that C_2H_4 and CH_3CHO are probably the primary products, with HCHO and CO as the secondary products. Moreover, the increased selectivity of HCHO corresponds better with the decreased selectivity of C_2H_4 than with that of CH_3CHO at 873 K. Thus it is likely that HCHO may be produced mainly from the consecutive oxidation of C_2H_4 over the MoO_x/SBA-15 catalyst.

It is noteworthy that the HCHO formed over the Cs-modified VO_x/SiO_2 or the $FePO_4$ catalyst during the selective oxidation of C_2H_6 by O_2 or N_2O was reported to stem from CH_3CHO [14,36,37]. To the best of our knowledge, there is no report showing that HCHO can be produced in considerable amounts from the oxidation of C_2H_4 by O_2. To gain further insight into whether HCHO comes mainly from C_2H_4 over our MoO_x/SBA-15 catalyst, we performed catalytic oxidation of C_2H_4 by O_2. As shown in Table 3, the main product in the oxidation of C_2H_4 by O_2 over the 20.1 wt% MoO_x/SBA-15

Table 3
The oxidation of ethylene by O_2 over the 20.1 wt% MoO_x/SBA-15 catalyst under different conditions

T (K)	W/F (s g cm^{-3})	Conversion (%)	Selectivity (%)				HCHO yield (%)
			CH_3CHO	HCHO	CO	CO_2	
803	0.046[a]	0.77	24	64	11	1.8	0.50
823	0.046[a]	7.8	12	73	12	1.9	5.6
843	0.046[a]	20	6.5	70	20	3.2	14
863	0.046[a]	30	3.2	63	29	4.1	19
863	0.02[b]	14	11	74	12	2.9	10
863	0.06[b]	39	5.3	66	24	4.6	26
863	0.12[b]	51	3.2	62	30	4.2	31

[a] Partial pressures of C_2H_4 and O_2, 7.8 kPa.
[b] Partial pressures of C_2H_4 and O_2, 10.1 kPa.

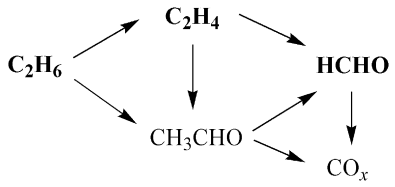

Scheme 1. Reaction paths in the selective oxidation of ethane by O_2 over the MoO_x/SBA-15 catalyst.

catalyst at different temperatures was HCHO. CH_3CHO with a lower selectivity was also formed. Table 3 also shows that the decrease in W/F increases the selectivity to both HCHO and CH_3CHO, indicating that HCHO and CH_3CHO may be formed in parallel from C_2H_4. However, our present results cannot completely exclude the possibility that HCHO may be formed from C_2H_4 through CH_3CHO. Considering these possibilities, we speculate that the reaction paths during the oxidation of C_2H_6 by O_2 over the MoO_x/SBA-15 catalyst may be expressed by Scheme 1.

4. Discussion

We have investigated both structural and catalytic properties of the MoO_x/SBA-15 catalysts with varying Mo content. Our results of structural characterizations reveal that the sample with Mo content <9.5 wt% contains mainly highly dispersed MoO_x species located inside the mesoporous channels of SBA-15. The analyses of H_2-TPR and diffuse reflectance UV–vis results further suggest that monomeric MoO_x species exist mainly in the catalysts with Mo content of 2.8 and 4.9 wt%, and that an increase in Mo content from 4.9 to 9.5 wt% causes the formation of two-dimensional MoO_x oligomers or small, three-dimensional polymeric MoO_x clusters in the mesoporous channels of SBA-15.

The characterizations with N_2-sorption, XRD, SEM, and TEM all show that the increase in Mo content to >15.4 wt% destroyed the ordered mesoporous structure of SBA-15 and caused the appearance of MoO_3 crystallites. It is worth mentioning that, although small amounts of big plate-like or belt-like MoO_3 crystallites were observed in the catalysts with Mo content of 15.4 and 20.1 wt%, these two catalysts have very different H_2-TPR profiles from crystalline MoO_3. The edge energy values evaluated from UV–vis spectra for these two catalysts, which reflect the average size of MoO_x domains, are also significantly higher than that for MoO_3 (∼2.9 eV), indicating that the average sizes of MoO_x domains for these two samples are smaller than that for crystalline MoO_3. Using TEM, we observed the growth of MoO_x species to MoO_x nanoparticles of 10–20 nm and the simultaneous collapse of the silica wall of SBA-15 for the catalysts with Mo content of 15.4 and 20.1 wt%. Based on these observations, we speculate that polymeric MoO_x clusters and MoO_x nanoparticles are the dominant molybdenum species in these catalysts. A further increase in Mo content to 23.5 wt% led to the formation of a larger number of thin needle-like MoO_3 crystallites. It is noteworthy that we have carried out characterizations with XRD, UV–vis, and TEM for some catalysts after reactions under the conditions shown in Fig. 9 for ∼6 h, and observed no significant changes in the structural features.

Catalytic studies showed that the conversion of C_2H_6 by O_2 increased gradually with increasing Mo content up to 6.6 wt%, while the rate of C_2H_6 conversion per Mo atom decreased slightly at the same time. A significant rise in C_2H_6 conversion was observed as Mo content exceeded 6.6 wt%, with the highest C_2H_6 conversion obtained over the catalyst with a Mo content of 20.1 wt%. The rate of C_2H_6 conversion per Mo atom became significantly greater over the catalyst with Mo content of 9.5–20.1 wt% compared with the catalyst with Mo content of 2.8–6.6 wt%. The correlation of these results with the structural features described above suggests that the polymeric MoO_x clusters or MoO_x nanoparticles have significantly higher activity toward C_2H_6 activation than the monomeric MoO_x species. The further increase in Mo content to 23.5 wt% decreased the conversion of C_2H_6 (Fig. 9) and the rate of C_2H_6 conversion per Mo atom simultaneously dropped significantly (Fig. 10), probably because most of the MoO_x species were aggregated to the needle-like MoO_3 crystallites.

Chen et al. [26,27] reported that the activity per Mo atom for the oxidative dehydrogenation of C_3H_8 increases with the size of MoO_x domains over the Al_2O_3-, ZrO_2-, or MgO-supported MoO_x catalysts, and they proposed that the reducibility of MoO_x species plays a key role in alkane activation. We evaluated H_2 reduction rates in the initial stage based on the data shown in Fig. 5 with a method reported by Chen et al. [27]. The H_2 reduction rate at 830 K, where oxygen conversion was <10% for all of the samples investigated, was calculated from the H_2 conversion at this temperature and the space velocity of H_2 (28 mmol H_2 per mol-Mo atom per second). It should be noted that the number of Mo atoms had been kept constant in H_2-TPR experiments by regulating the amount of catalyst, and the quantification of H_2 conversion was carried out using the reduction of CuO powder as the standard. The calculated rates of H_2 reduction for catalysts with different Mo content are plotted in Fig. 10. Similar trends observed for the changes in the rates of C_2H_6 conversion and H_2 reduction with Mo content strongly suggest that the reducibility of MoO_x species is crucial in determining the rate of C_2H_6 conversion over our catalysts.

As described previously, studies on the selective oxidation of C_2H_6 by O_2 to organic oxygenates using supported MoO_x

catalysts are unexpectedly scarce. Over our MoO_x/SBA-15 catalysts, CH_3CHO and HCHO were produced along with C_2H_4 and CO_x. More significantly, our results suggest that the selective formation of these two oxygenates requires different structures of MoO_x species. The catalysts with lower Mo content (2.8–6.6 wt%) favor the selectivity of CH_3CHO, whereas those with higher Mo content (15.4 and 20.1 wt%) are beneficial to the formation of HCHO. This is also the case even when the product distributions are compared at the same C_2H_6 conversion level. As an example, at a fixed C_2H_6 conversion of 7.3% (obtained by changing the W/F value at 873 K), the selectivities to CH_3CHO and HCHO were 22 and 15%, respectively, over the 6.6 wt% MoO_x/SBA-15 catalyst, compared with 6.3 and 29% over the 20.1 wt% MoO_x/SBA-15 catalyst. Therefore, it is reasonable to conclude that the highly dispersed MoO_x species (probably including monomeric and oligomeric MoO_x species) can provide higher selectivity to CH_3CHO, whereas polymeric MoO_x clusters and MoO_x nanoparticles account for the formation of HCHO with higher selectivity. The highest yields to CH_3CHO and HCHO at 873 K reached 0.94 and 4.2% over the MoO_x/SBA-15 catalysts with Mo content of 9.5 and 20.1 wt%, respectively. Such a high single-pass HCHO yield has never been reported in the oxidation of C_2H_6.

The kinetic studies suggest that C_2H_4 is a primary product from C_2H_6 oxidation, whereas CH_3CHO may be a primary product from C_2H_6 or may be formed from C_2H_4 oxidation. It is likely that HCHO is produced mainly from the oxidation of C_2H_4 over our MoO_x/SBA-15 catalyst, but CH_3CHO also may be an intermediate product during HCHO formation. We speculate that the rapid consecutive oxidation of CH_3CHO over the catalyst with a higher Mo content may be responsible for its lower selectivity to CH_3CHO, whereas the catalyst with highly dispersed MoO_x species may prevent further oxidation of CH_3CHO to some extent. On the other hand, the consecutive oxidation of HCHO may proceed much slower even over the catalyst with polymeric MoO_x clusters or MoO_x nanoparticles. Further studies on the catalyst requirements for the oxidation of C_2H_4 to HCHO by O_2 are underway in our laboratory.

5. Conclusion

The structure of MoO_x species introduced into SBA-15 changes significantly with Mo content. At Mo content <9.5 wt%, the ordered mesoporous structure of SBA-15 can be well sustained, and most of the MoO_x species are highly dispersed in the mesoporous channels of SBA-15. The catalysts with Mo content of 2.8 and 4.9 wt% contain mainly monomeric MoO_x species, and the increase in Mo content to 9.5 wt% causes the formation of oligomeric MoO_x species or polymeric MoO_x clusters. Further increases in Mo content to >15.4 wt% cause the collapse of the ordered mesoporous structure and the appearance of crystalline MoO_3. However, the catalysts with Mo content of 15.4 and 20.1 wt% comprise only a small amount of plate-like or belt-like MoO_3 crystallites, and MoO_x nanoparticles of 10–20 nm are mainly observed. The growth of the MoO_x species in the mesoporous channels to MoO_x nanoparticles results in the collapse of the silica wall of SBA-15. The conversion of C_2H_6 increases with Mo content and reaches a maximum at a Mo content of 20.1 wt%. The catalyst with Mo content of 9.5–20.1 wt% exhibits a significantly higher rate of C_2H_6 conversion per Mo atom than that with a lower Mo content, suggesting that the polymeric MoO_x clusters or MoO_x nanoparticles are more active toward C_2H_6 activation. We have confirmed that the higher reducibility of these MoO_x species accounts for the higher rate of C_2H_6 conversion. HCHO and CH_3CHO can be obtained during the oxidation of C_2H_6 by O_2 over the MoO_x/SBA-15 catalysts, and the selectivities of the two products are strongly dependent on the structure of MoO_x species. The selective formation of CH_3CHO is favored over the catalysts with highly dispersed MoO_x species, whereas the formation of HCHO with a higher selectivity (∼30%) requires the presence of polymeric MoO_x clusters or MoO_x nanoparticles. Single-pass HCHO yields >4% can be obtained over the 20.1 wt% MoO_x/SBA-15 catalyst, and it is likely that HCHO is formed mainly through the catalytic oxidation of C_2H_4 by O_2.

Acknowledgments

This work was supported by the National Natural Science Foundation of China (grants 20433030 and 20625310), the National Basic Research Program of China (grants 2005CB221408 and 2003CB615803), the Program for New Century Excellent Talents in University of China (grant NCET-04-0602), and the Key Scientific Project of Fujian Province of China (grant 2005HZ01-3).

References

[1] H.-F. Liu, R.-S. Liu, K.Y. Liew, R.E. Johnson, J.H. Lunsford, J. Am. Chem. Soc. 106 (1984) 4117.
[2] R. Pitchai, K. Klier, Catal. Rev. Sci. Eng. 28 (1986) 13.
[3] N.D. Spencer, J. Catal. 109 (1988) 187.
[4] N.D. Parkyns, C.I. Warburton, J.D. Wilson, Catal. Today 18 (1993) 385.
[5] T.J. Hall, J.S.J. Hargreaves, G.J. Hutchings, R.W. Joyner, S.H. Taylor, Fuel Process. Technol. 42 (1995) 151.
[6] K. Otsuka, Y. Wang, Appl. Catal. A 222 (2001) 145.
[7] K. Tabata, Y. Teng, T. Takemoto, E. Suzuki, M.A. Banares, M.A. Pena, J.L.G. Fierro, Catal. Rev. 44 (2001) 1.
[8] F. Arena, A. Parmaliana, Acc. Chem. Res. 36 (2003) 867.
[9] M. Baerns, O. Buyevskaya, Catal. Today 45 (1998) 13.
[10] M.A. Bañares, Catal. Today 51 (1999) 319.
[11] L. Mendelovici, J.H. Lunsford, J. Catal. 94 (1985) 37.
[12] A. Erdőhelyi, F. Máté, F. Solymosi, J. Catal. 135 (1992) 563.
[13] S.T. Oyama, J. Catal. 128 (1991) 210.
[14] Z. Zhao, Y. Yamada, Y. Teng, A. Ueda, K. Nakagawa, T. Kobayashi, J. Catal. 191 (2000) 215.
[15] T. Kobayashi, Catal. Today 71 (2001) 69.
[16] Z. Zhang, Z. Zhao, C. Xu, Chin. Sci. Bull. 50 (2005) 833.
[17] Y. Murakami, K. Otsuka, Y. Wada, Bull. Chem. Soc. Jpn. 63 (1990) 340.
[18] R.B. Watson, U.S. Ozkan, J. Catal. 208 (2002) 124.
[19] M.A. Bañares, J.L.G. Fierro, in: T. Oyama, J.W. Hightower (Eds.), Catalytic Selective Oxidation, in: ACS Symp. Ser., vol. 523, Am. Chem. Soc., Washington, DC, 1993, p. 354.
[20] M.R. Smith, L. Zhang, S.A. Driscoll, U.S. Ozkan, Catal. Lett. 19 (1993) 1.
[21] K. Suzuki, T. Hayakawa, M. Shimizu, K. Takehira, Catal. Lett. 30 (1993) 167.
[22] M. Faraldos, M.A. Bañares, J.A. Anderson, H. Hu, I.E. Wachs, J.L.G. Fierro, J. Catal. 160 (1996) 214.

[23] T. Sugino, A. Kido, N. Azuma, A. Ueno, Y. Udagawa, J. Catal. 190 (2000) 118.
[24] N. Ohler, A.T. Bell, J. Catal. 231 (2005) 115.
[25] N. Ohler, A.T. Bell, J. Phys. Chem. B 110 (2006) 2700.
[26] K. Chen, S. Xie, A.T. Bell, E. Iglesia, J. Catal. 198 (2001) 232.
[27] K. Chen, A.T. Bell, E. Iglesia, J. Catal. 209 (2002) 35.
[28] D. Zhao, J. Feng, Q. Hu, N. Melosh, G.H. Fredrickson, B.F. Chmelka, G.D. Stucky, Science 279 (1998) 548.
[29] Y.M. Liu, Y. Cao, N. Yi, W.L. Feng, W.L. Dai, S.R. Yan, H.Y. He, K.N. Fan, J. Catal. 224 (2004) 417.
[30] Y. Wang, X. Wang, Z. Su, Q. Guo, Q. Tang, Q. Zhang, H. Wan, Catal. Today 93–95 (2004) 155.
[31] V. Fornés, C. López, H.H. López, A. Martínez, Appl. Catal. A 249 (2003) 345.
[32] D.A. Ruddy, N.L. Ohler, A.T. Bell, T. Don Tilley, J. Catal. 238 (2006) 277.
[33] W. Yang, X. Wang, Q. Guo, Q. Zhang, Y. Wang, New J. Chem. 27 (2003) 1301.
[34] H. Hu, I.E. Wachs, S.R. Bare, J. Phys. Chem. 99 (1995) 10897.
[35] R.S. Weber, J. Catal. 151 (1995) 470.
[36] Y. Wang, K. Otsuka, J. Chem. Soc. Faraday Trans. 91 (1995) 3953.
[37] Y. Wang, K. Otsuka, J. Catal. 171 (1997) 106.
[38] Z. Zhang, Z. Zhao, C. Xu, A. Duan, A. Sha, Y. Zhang, T. Dou, Chem. Lett. 34 (2005) 1080.